Mark M. Plecnik[1]
Biomimetic Millisystems Lab,
Department of Electrical Engineering and
Computer Sciences,
University of California,
Berkeley, CA 94720
e-mail: mplecnik@berkeley.edu

Duncan W. Haldane
Biomimetic Millisystems Lab,
Department of Mechanical Engineering,
University of California,
Berkeley, CA 94720
e-mail: dhaldane@berkeley.edu

Justin K. Yim
Biomimetic Millisystems Lab,
Department of Electrical Engineering and
Computer Sciences,
University of California,
Berkeley, CA 94720
e-mail: yim@eecs.berkeley.edu

Ronald S. Fearing
Professor
Biomimetic Millisystems Lab,
Department of Electrical Engineering and
Computer Sciences,
University of California,
Berkeley, CA 94720
e-mail: ronf@eecs.berkeley.edu

Design Exploration and Kinematic Tuning of a Power Modulating Jumping Monopod

The leg mechanism of the novel jumping robot, Salto, is designed to achieve multiple functions during the sub-200 ms time span that the leg interacts with the ground, including minimizing impulse loading, balancing angular momentum, and manipulating power output of the robot's series-elastic actuator. This is all accomplished passively with a single degree-of-freedom linkage that has a coupled, unintuitive design which was synthesized using the technique described in this paper. Power delivered through the mechanism is increased beyond the motor's limit by using variable mechanical advantage to modulate energy storage and release in a series-elastic actuator. This power modulating behavior may enable high amplitude, high frequency jumps. We aim to achieve all required behaviors with a linkage composed only of revolute joints, simplifying the robot's hardware but necessitating a complex design procedure since there are no pre-existing solutions. The synthesis procedure has two phases: (1) design exploration to initially compile linkage candidates, and (2) kinematic tuning to incorporate power modulating characteristics and ensure an impulse-limited, rotation-free jump motion. The final design is an eight-bar linkage with a stroke greater than half the robot's total height that produces a simulated maximum jump power 3.6 times greater than its motor's limit. A 0.27 m tall prototype is shown to exhibit minimal pitch rotations during meter high test jumps. [DOI: 10.1115/1.4035117]

1 Introduction

We present the design of a leg mechanism for a monopedal jumping robot that transforms motor torque into a high-powered vertical force by manipulating power transmission through a spring element; see Fig. 1. A two-phased approach is employed that includes (1) design exploration and (2) kinematic tuning. In addition to manipulating series-elastic power output, the mechanism functions to reduce gear train requirements, minimize impulse loading, and jump with near-zero angular velocity. These functions are accomplished by synthesizing the leg linkage to achieve a set of kinematic and dynamic behaviors. Required behaviors include that the robot's foot trace a straight line, that its input-output links move according to a specified mechanical advantage, that it pushes with a constant ground reaction force, that it minimizes moments on its body, and other behaviors which are formally introduced in the proceeding sections. Control of spring energy is accomplished by tuning a variable mechanical advantage curve over the stroke of the mechanism to increase power delivered to the foot beyond the sustainable limit of the motor, a strategy we refer to as *power modulation*. The intent of our leg design is to enable a novel robotic platform, named Salto, to perform high amplitude, high frequency jumps [1].

In order to achieve a list of primary behaviors, design exploration is performed by computing an atlas of over 90 Stephenson six-bar linkages that trace a near-perfect straight line. This atlas provides a list of starting mechanisms suitable for kinematic tuning through optimal synthesis theory. Kinematic tuning then achieves an extended list of more intricate behaviors; see Fig. 2. During kinematic tuning, we found that extra links must be added to balance angular momentum, making the final design a single degree-of-freedom eight-bar linkage. A prototype of Salto's leg produces a 0.15 m stroke on a 0.27 m tall robot. Meter high test jumps of the prototype exhibited minimal pitch rotations.

2 Background

2.1 Mechanism Design. A common approach to engineering design problems is to select viable candidates from a database of pre-existing solutions to move forward into a detailed design or

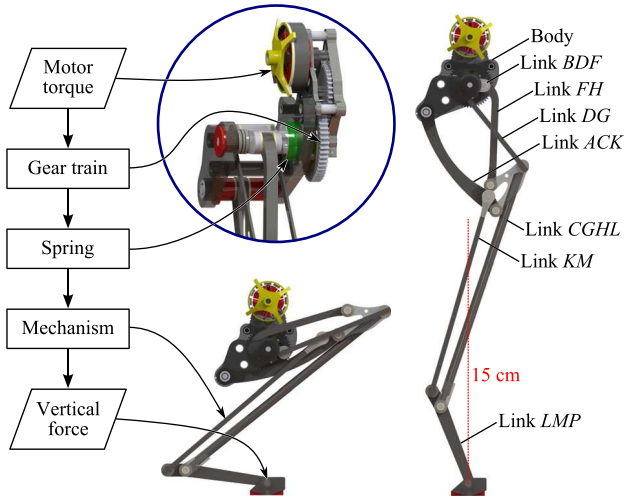

Fig. 1 The leg design of Salto transforms motor torque into a tuned vertical ground reaction force

[1]Corresponding author.

Manuscript received April 29, 2016; final manuscript received October 27, 2016; published online December 7, 2016. Assoc. Editor: Sarah Bergbreiter.

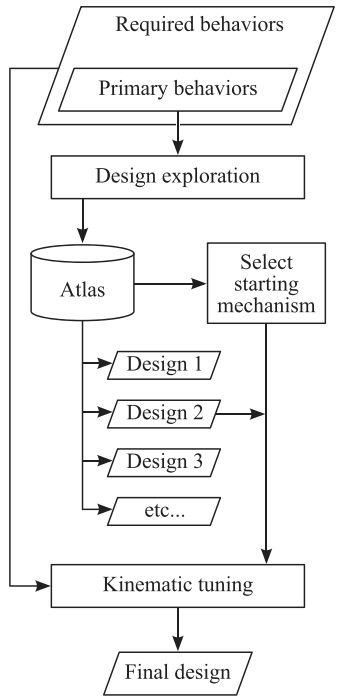

Fig. 2 The design process consists of design exploration and kinematic tuning phases

analysis phase. This practice is found in the design of drugs [2–5], chemicals [6,7], integrated circuits [8,9], actuators [10], composite materials [11], multiagent games [12], packaging structures [13], telecommunication networks [14,15], and microarray experiments [16] where some research focuses on enumerating the space of possible designs while others focus on searching through existing databases. The design exploration of mechanisms adopted the strategy of design atlases early on including Brown's *Five Hundred and Seven Mechanical Movements* [17], through Reuleaux's famous educational models [18,19], then the well-worn four-bar atlas from Hrones and Nelson [20] at the mid 20th century, toward its software accompanied reincarnation today [21]. As well, today the Reuleaux models and other collections have manifested themselves in online digital libraries [22–24] to serve as idea banks for mechanical designers.

The literature on design exploration using mechanism atlases can be divided into graph theory-based enumerations of linkage topologies [25–28] and dimensional synthesis [29], which is the topic of the current work. Existing atlases for dimensional synthesis focus on the coupler curves of planar four-bars [20,21], spherical four-bars [30,31], spatial four-bars [32], and planar geared five-bars [33,34]. These atlases are created by sampling the entirety of a space of design parameters (linkage dimensions) and recording coupler curves along the way as spline parameters [35,36], polygons [34], or more commonly Fourier coefficients [30–32,37,38]. The existing literature is restricted to four- and five-bars defined by up to eight parameters with the exception of [37,38], which report the use of six-bar atlases and [34] which suggests a 12 parameter space was sampled using a Poisson-disk method. However, these works do not disclose the parameterizations that were used.

In the current work, we consider the space of planar six-bar linkages which could be cataloged by a minimum of 11 parameters after normalizing rotations, translations, and scalings, e.g., Fig. 3. Naively storing all combinations of ten different values for each design parameter would require the analysis of 10^{11} linkages, with which a computational setup that analyzes 10,000 linkages per second would finish in just over 115 days. The extensibility of this technique is not optimistic and resolution would be questionable for the increased nonlinearity of six-bar linkage coupler curves [39].

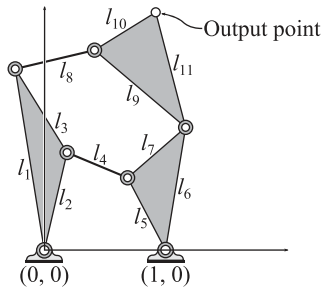

Fig. 3 A parameterization of a six-bar linkage that results in 11 design parameters

As echoed in many of the references above, atlas-based solutions provide effective start points for detailed design/optimization [40,41] rather than final designs in themselves. We adopt this strategy as well except we propose atlas compilation on a per case basis by retrieving the subset of linkages that produce a primary set of kinematic behaviors, circumventing the problem of sampling the entire space. In what follows, we demonstrate how Stephenson six-bars that trace a straight line can be compiled by solving large polynomial systems to form an atlas for the design of a leg mechanism of a jumping robot. A mechanism is selected from this atlas and adapted via gradient descent optimization into a solution which simultaneously produces multiple required behaviors. During kinematic tuning, extra links are added converting our linkage solution into an optimized eight-bar in order to resolve mass balancing issues of the jumping mechanism.

2.2 Jumping Mechanisms. The Salto leg mechanism simultaneously accomplishes multiple functions. The most fundamental of these is to transform motor torque into a vertical ground reaction force greater than the robot's weight. In order to compare our work to prior literature, we list four other functions:

A. The mechanism reduces the required output torque from the motor/gear train.
B. Desired take-off velocity is achieved with peak accelerations minimized.
C. The robot jumps with near-zero angular velocity.
D. Transient power output of a series-elastic actuator is modulated to increase jump energy.

By simultaneously producing all of the above functions, our design is set apart from the myriad of novel jumping robots produced over the past few decades. Recounting these works reveals a diverse set of approaches including mechanisms based on single prismatic legs [42], spring-loaded hinges [43], cam/pulley systems [44], four-bars [45–54], cam-actuated four-bars [55–58], a serial chain that forms an instantaneous four-bar [59], a spatial four-bar [60], five-bars [61,62], single-loop symmetric six-bars [63–65], a rack-and-pinion [66], a Sarrus linkage [67], serial chains [68,69], wire-driven serial chains [70–72], bistable mechanisms [73,74], closed elastica [75,76], winch-retracted leaf springs [77,78], symmetric elastic structures [79–83], and inflatable silicone air chambers [84]. None of these robots consider all of the functions listed above. Below we recount their functional considerations, independent of how well they were achieved.

A. Motor/gear train reduction: Several jumping robot designs have considered reducing the required force/torque to be produced by the motor and gear train [51–53,62,65, 72,76,77,83], often employing cams to assist in storing spring energy [44,55,56,59,79].

B. Peak accelerations minimized: Works that have considered the influence of mechanism design on the ground reaction force (GRF) include [42,45,50,52,54,62,67–69,80] with many approaching this problem from the perspective of eliminating premature take-off [49,55–57,63,65,73,83], that is when the vertical

component of the ground force vanishes before the leg has fully extended. Closer to our work, a few researchers have considered or implemented mechanisms that accomplish near-constant acceleration of their robots [55,60,72,77,79]. This solution both eliminates premature take-off and achieves take-off velocity with a minimally impulsive GRF. Multiple works recognize the benefit of reduced peak loading, and a few works [52,55,62,82] mention the utility of long leg extension to achieve this objective which was motivated in Ref. [79]. This feature is implicit in several designs which exhibit a large *stroke ratio*, i.e., the quotient of vertical center of mass (CM) translation during stance to mechanism length at full extension. The stroke ratio was on average 50% as roughly estimated from Refs. [44–49,51,53,56–60,62–64,66,71–73,76,79–82], and 67% for Salto's leg; see Fig. 1. Note that the stroke ratio is computed from the mechanism length which does not include the motor's dimensions.

C. Rotation-free jump: Several works explicitly consider the effect of mechanism design on rotation-free jumping [43,49,52,57,59,70,72,77] and several more possess this feature implicitly through symmetry [42,51,53,62–65,79–83]. Others resort to self-righting mechanisms after landing [43,50,56,57,63,65,79,81,83], aerodynamic stabilization [51,79], or active control [54,68,69].

D. Series-elastic power modulation: Robots that employ series-elastic actuation to perform jumping maneuvers include [68,85,86]. Salto differs from these robots in that it produces a mechanical advantage profile that couples with a series-elastic actuator to enable transient energy storage and increase jump power. To a degree, power modulation occurs in any leg system with compliance, but never before has it been precisely designed.

In terms of design goals, our work is related to the GRILLO III robot [60]. This robot imitates the kinematics and dynamics of the leg of the leafhopper insect, *Cicadella viridis*, to achieve a constant GRF and straight-line path generation at the foot [87]. As well, GRILLO III's designers accurately identify the role of variable mechanical advantage in power modulation of bullfrog legs [55], but do not provide a solution for series-elastic power modulation in robots.

The mechanical advantage of an ideal mechanism is its ratio of output to input force/torque which generally varies over linkage configurations. Several of the works above note benefits gained from the variable mechanical advantage of their chosen linkage systems [49,51,52,55,60,62,63,67,72,73]. Our work is different in that we do not investigate the benefits of generically chosen linkages or from dimensions chosen to mimic animals; rather, we use dimensional synthesis theory to precisely synthesize the mechanism behaviors required to perform the aforementioned functions. Our instance of bio-inspiration comes from considering the power modulation strategy through literature on *Galago senegalensis* [88]. That said, we present the first jumping mechanism with a specially designed mechanical advantage profile that modulates the power output of a series-elastic actuator to considerably increase jump energy.

Power modulation occurs when mechanical power output exceeds the peak power of an actuator. For wind-up mechanisms, power modulation occurs as discrete charging and uncharging events using a latch to decouple and recouple a parallel-elastic structure. System compliance is a prerequisite for power modulation. We choose to implement a series-elastic structure, which has been studied in Ref. [89] as a simple actuator-spring-mass system under the effects of gravity. This work reports the maximum ratio of mechanical power to peak actuator power, a metric termed the *power modulation factor*, is 2.0. To move beyond this limit requires variable mechanical advantage. Salto has a mechanical advantage profile specifically tuned for series-elastic power modulation and achieves a power modulation factor of 3.6 in simulation. In other works, we show how power modulation leads to vertical jumping agility and enables acrobatic maneuvers [1,90]. Salto was designed using new algorithms in dimensional synthesis theory, allowing a rigorous exploration of the kinematic design space which has not yet been achieved for a jumping robot.

In the proceeding, we present the required behaviors in Sec. 3, discuss design exploration via atlas compilation in Sec. 4, then describe how required behaviors are tuned simultaneously using optimal synthesis theory in Secs. 5 and 6. Section 7 describes the construction of a prototype and experimental results are given in Sec. 8.

3 Required Behaviors

In this section, we decompose the functions listed in Sec. 2.2 into required behaviors of the kinematics and dynamics of the mechanism. Our use of the words *functions* and *behaviors* follows [91]. The required behaviors are as follows:

(1) The mechanism constrains a foot point to a vertical straight line, the *line-of-action*, in the frame of the robot.
(2) Translation of the foot point, or *stroke*, is long relative to the size of the robot.
(3) All pivots are located above the foot point at all times, with an input pivot near to the line-of-action.
(4) Link lengths are compact.
(5) The input link that attaches to the series-elastic actuator rotates over a large range.
(6) The leg possesses low mechanical advantage at the top of stroke.
(7) Mechanical advantage defines a constant ground force for the remainder of stroke.
(8) Moments exerted on the body of the robot by the mechanism are minimized.

We term behaviors 1–4 as the *primary behaviors*. In order to create a nearly vertical GRF, Req. 1 specifies the foot path to trace a straight vertical line in the frame of the robot body. Lateral movement of the foot will incite a horizontal component of the GRF, adding undue angular momentum to the system. Even with a perfectly straight foot path, inertial forces of the moving links will deviate the GRF from the line-of-action however, so long as their horizontal resultant is small, the direction of the GRF will be dominated by the line-of-action. Req. 2 specifies a long foot stroke in order to increase the acceleration time of the robot, i.e., when the foot is in contact with the ground. Increasing this time decreases the acceleration and power required to achieve a given take-off velocity. Req. 3 disqualifies geometries that interfere with the ground and positions the input pivot, which locates the substantial mass of the motor, close to the line-of-action. Req. 4 seeks to obtain designs without protruding links that may collide with the environment. Linkages that produce these four primary behaviors are sought during design exploration; see Fig. 2.

Upon choosing a suitable design from this exploration, the remaining behaviors are achieved using a kinematic tuning procedure based on optimization theory. Req. 5 essentially adds an extra gear reduction by specifying the input link to move over a greater angular displacement (at higher angular velocity) during mechanism stroke, reducing the required gearbox gear reduction on the motor. Reqs. 6 and 7 enable power modulation. By specifying mechanical advantage to be low at the top of stroke, Req. 6 essentially multiplies the weight of the robot so that the motor can operate near its stall torque, transferring energy into the series-elastic spring element. Although mechanical advantage is low, it is specified to be nonzero so that the motor never actually stalls. Once the leg extends past this low region, an increase in mechanical advantage triggers high-powered energy transfer from the spring into vertical motion. Since Hooke's law dominates the series-elastic torque at this portion of the mechanism's stroke, Req. 7 specifies mechanical advantage to be a map from the unwinding spring torque to a constant force at the foot. By implementing constant acceleration, the robot achieves a given take-off velocity with minimal peak accelerations, i.e., no isolated peaks.

Finally, Req. 8 specifies balanced angular momentum to ensure the robot does not rotate after the foot breaks ground contact. Although preceding behaviors place both the CM and GRF approximately on the line-of-action, the addition of moving link

inertias causes horizontal accelerations of the CM and thus horizontal components of the GRF, adding angular momentum to the system. Therefore, the final stage of kinematic tuning involves balancing angular momentum of the moving links to produce a rotation-free jump. Furthermore, we take this requirement a step further by specifying the body link, the majority of the robot's mass, to have almost no moment exerted on it. This feature ensures that airborne leg extension does not apply a torque to the body link.

4 Design Exploration

To accumulate an atlas of starting mechanisms, we explore the space of planar linkages that trace an exact or approximate straight line. Cams, gears, and sliders are ruled out to avoid weight, wear, and complexity. An atlas of straight-line four-bars appears in Ref. [92] , but it does not contain linkages with pivots in satisfactory locations (Reqs. 3 and 4). This list includes the symmetric four-bars of Watt, Roberts, and Chebyshev. An example of a best-fit straight-line four-bar with ground pivots in satisfactory locations is described in Ref. [45]. However, this design does not produce Reqs. 1 and 2 as it traces an arc with a stroke ratio of 27%. Furthermore, four-bar linkages have a limited number of design parameters which would make it difficult to include additional behaviors during optimization-based kinematic tuning.

Therefore, we advance to one degree-of-freedom six-bar linkages, an incremental step that results in huge growth of the design space to explore. This growth is due to adding six new dimensions (planar coordinates of three new pivots), an increase in nonlinearity, and the addition of multiple kinematic inversions. Quantifications of the size of this space are given in Ref. [93] from which we also use a design procedure for exploring Stephenson six-bars.

This procedure discovers all Stephenson linkages designed as constrained revolute-revolute (RR) chains that trace a straight line. First, an RR chain is specified along with path control points. Solving the inverse kinematics of the RR chain determines the joint angle coordination necessary to trace through the control points. This coordination is accomplished through a Stephenson function generator, of which a huge number of design options exist. This design space is effectively explored through encoding motion requirements as massive polynomial systems with roots that correspond to linkage design candidates. Solving these systems [94,95] finds complete sets of design candidates which are then analyzed to eliminate linkage defects. The resulting atlas of design options can be browsed to determine the best design(s).

Control points were chosen for an RR chain pinned at the origin with link lengths 2 and 2.5 to trace through (x, y) coordinates:

$$\{(0,-0.8),\ (0,-1.125),\ (0,-1.5),\ (0,-1.875),\ (0,-2.25),\ (0,-2.625),\ (0,-3),\ (0,-3.375),\ (0,-3.75),\ (0,-4.125),\ (0,-4.4)\} \quad (1)$$

Note that, for now, dimensions are not assigned units and can be considered ratios.

This exploration discovered 2986 Stephenson I, 578 Stephenson II (binary), 804 Stephenson II (ternary), and 110 Stephenson III linkages that trace through control points without branch or circuit defects. Schematics of the four types of Stephenson path generators are shown in Fig. 4. These results demonstrate the capability of six-bars to draw straight lines.

In order to create a useful atlas, we process results by removing linkages with excessively long link lengths and grouping the remainder into sets of similar designs. Two designs were considered similar if the norm of the difference of vectors of pivot locations was less than a threshold value, in this case 2. The number of sets of similar designs found for each type was 43 for Stephenson I, 22 for Stephenson II (binary), 7 for Stephenson II (ternary), and 4 for Stephenson III. The compilation of these solution sets forms an atlas of viable start points for any optimization procedure. Samples from this atlas are shown in Fig. 5. As an interesting aside, the mechanism shown in Fig. 5(*a*) resembles a cognate of Hart's *second* straight-line mechanism, which is currently the only Stephenson linkage known to trace an exact straight line [96].

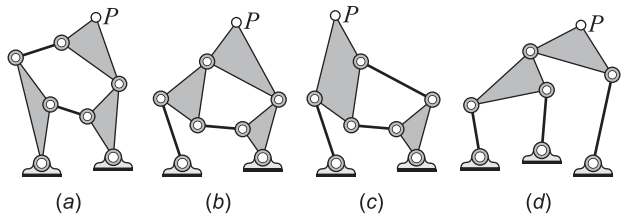

Fig. 4 Four types of Stephenson path generating six-bars: (*a*) Stephenson I, (*b*) Stephenson II (binary), (*c*) Stephenson II (ternary), and (*d*) Stephenson III

We do not investigate every solution within this atlas but instead pick the Stephenson II (ternary) design shown in Fig. 5(*e*)

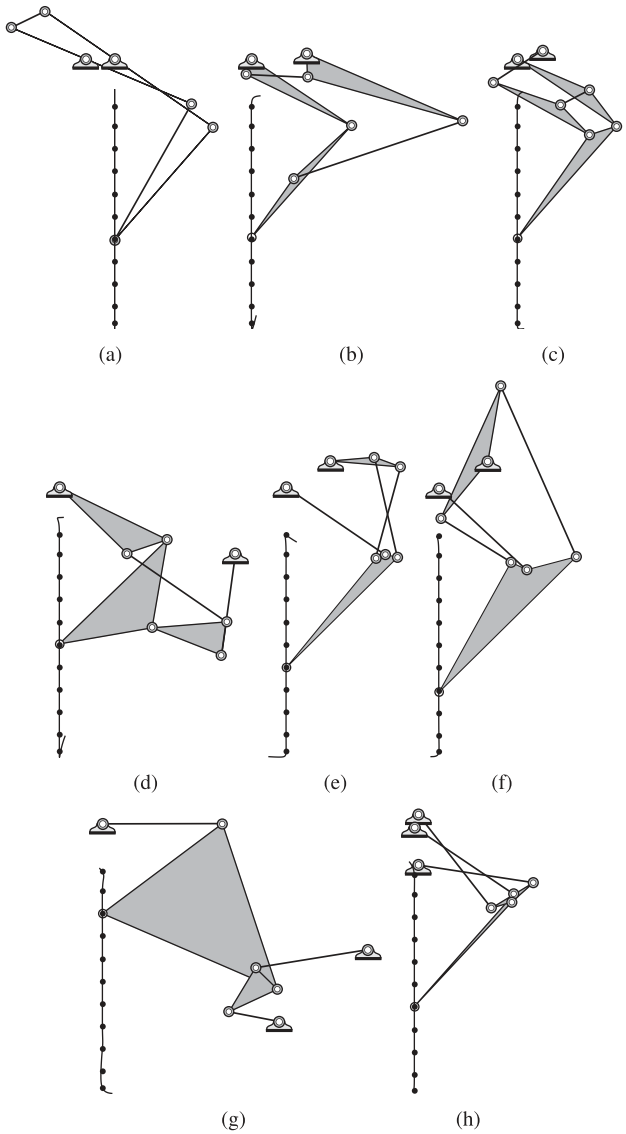

Fig. 5 Samples from an atlas of straight-line six-bars. Stephenson I types are shown in (*a*) and (*b*); Stephenson II (binary) types are shown in (*c*) and (*d*); Stephenson II (ternary) types are shown in (*e*) and (*f*); and Stephenson III types are shown in (*g*) and (*h*).

to further explore as it produces the primary behaviors and also produces Req. 5. The design procedure used above required us to specify the horizontal distance between the line-of-action and one of the fixed pivots. In order to generate more designs, we explore offsetting the line-of-action to the left and right of this pivot by 0.5 units and computing more Stephenson II (ternary) designs to add to our atlas. This found 3 and 14 more sets of similar designs for the left and right cases, respectively, see Fig. 6.

The design shown in Fig. 6(*b*) was selected as the optimization start point for kinematic tuning and so we call it Iteration I. This design produced the primary behaviors with compact dimensions and its actuated pivot (see Fig. 6(*b*)) near the line-of-action. Its straight-line motion is generated over 217 deg of rotation of the input link which strongly produced Req. 5, better than any other atlas design. The remaining behaviors are to be achieved during kinematic tuning described in Secs. 5 and 6.

5 Tuning: Six-Bar Optimization

The optimal design equations for a Stephenson II (ternary) type linkage were formulated to allow specification of the foot point path and/or input crank angle at an arbitrary number of positions. Coordination between the input crank and foot translation allows mechanical advantage to be defined over the mechanism's stroke in order to manipulate the storage and release of energy in the spring element during leg extension.

5.1 Formulation. We choose the design parameters for a Stephenson II linkage to be the coordinates of its pivots in a reference configuration. It has two ground pivots located by complex numbers $A = A_x + A_y i$ and $B = B_x + B_y i$. Similarly, it has five moving pivots that have fixed reference positions C, D, F, G, and H, which are also complex numbers. The foot trace point has reference position P_0. Connecting pivots as shown in Fig. 7 forms five links AC, CGH, BDF, DG, and FH, which when rotated from their reference configuration are measured by ϕ_j, ρ_j, ψ_j, θ_j, and μ_j in the jth configuration, respectively. Rotations are represented with the following exponential operators:

$$Q_j = e^{i\phi_j}, \quad R_j = e^{i\rho_j}, \quad S_j = e^{i\psi_j}, \; T_j = e^{i\theta_j}, \quad U_j = e^{i\mu_j} \tag{2}$$

The input link, as dictated by the starting mechanism selected from the atlas, is BDF measured by ψ_j.

The formulation begins by following three independent vector loops from ground to trace point P_j in the jth configuration,

$$A + Q_j(C - A) + R_j(P_0 - C) = P_j \tag{3}$$

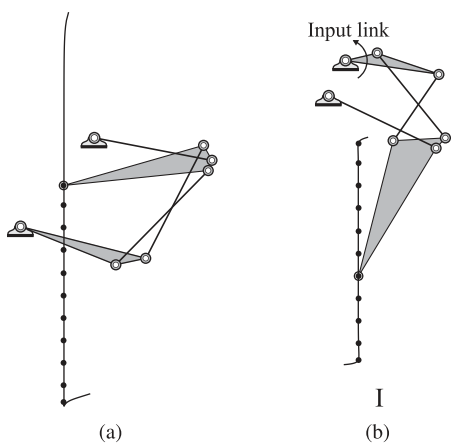

Fig. 6 Samples from an expanded atlas of Stephenson II (ternary) six-bars. The line-of-action was shifted to the left in (*a*) and shifted to the right in (*b*).

$$B + S_j(D - B) + T_j(G - D) + R_j(P_0 - G) = P_j \tag{4}$$

$$B + S_j(F - B) + U_j(H - F) + R_j(P_0 - H) = P_j \tag{5}$$

To facilitate presentation of the design equations, we define intermediate variables,

$$\begin{aligned} a_j &= A - P_j + Q_j(C - A) \\ b_j &= B - P_j + S_j(D - B) \\ c_j &= B - P_j + S_j(F - B) \end{aligned} \tag{6}$$

Exponential operators R_j, T_j, and U_j are eliminated from Eqs. (3), (4), and (5), respectively, by isolating R_j, T_j, and U_j terms on one side of each equation and then multiplying each equation by its complex conjugate to obtain,

$$a_j \bar{a}_j = (P_0 - C)(\bar{P}_0 - \bar{C}) \tag{7}$$

$$(b_j + R_j(P_0 - G))(\bar{b}_j + \bar{R}_j(\bar{P}_0 - \bar{G})) = (G - D)(\bar{G} - \bar{D}) \tag{8}$$

$$(c_j + R_j(P_0 - H))(\bar{c}_j + \bar{R}_j(\bar{P}_0 - \bar{H})) = (H - F)(\bar{H} - \bar{F}) \tag{9}$$

where the overbar denotes the conjugate. Then Eq. (3) is solved for R_j and substituted into Eqs. (8) and (9) to obtain

$$\begin{aligned} &(b_j(P_0 - C) - a_j(P_0 - G))(\bar{b}_j(\bar{P}_0 - \bar{C}) - \bar{a}_j(\bar{P}_0 - \bar{G})) \\ &\quad = (P_0 - C)(\bar{P}_0 - \bar{C})(G - D)(\bar{G} - \bar{D}) \end{aligned} \tag{10}$$

$$\begin{aligned} &(c_j(P_0 - C) - a_j(P_0 - H))(\bar{c}_j(\bar{P}_0 - \bar{C}) - \bar{a}_j(\bar{P}_0 - \bar{H})) \\ &\quad = (P_0 - C)(\bar{P}_0 - \bar{C})(H - F)(\bar{H} - \bar{F}) \end{aligned} \tag{11}$$

Equations (7), (10), and (11) represent the constrained geometry of a Stephenson II six-bar for the jth configuration and are denoted by $\mathcal{C}_j$. In addition to design parameters $\{A, B, C, D, F, G, H\}$, these equations contain unknown angles ϕ_j and ψ_j, and foot positions P_j. Desired foot positions are specified at N configurations as $\tilde{P}_j$, $j = 0, \ldots, N-1$, and desired crank angles as $\tilde{\psi}_j$, $j \in l$ where l

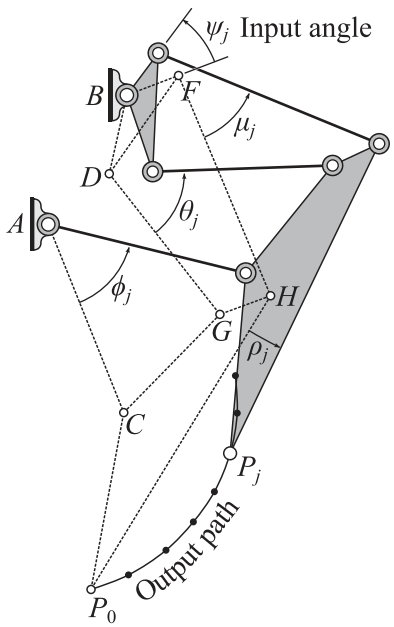

Fig. 7 A six-bar linkage defined by coordinates *A*, *B*, *C*, *D*, *F*, *G*, *H*, and P_0 drawn in configuration *j*

contains the indices of configurations where it is desired to specify crank angle. This allows us to construct the objective function

$$f = w_{\text{pt}} \sum_{j=0}^{N-1} ((\tilde{P}_j - P_j)(\tilde{\bar{P}} - \bar{P}_j)) + w_{\text{ang}} \sum_{j \in I} \left(\left(\cos \tilde{\psi}_j - \cos \psi_j \right)^2 + \left(\sin \tilde{\psi}_j - \sin \psi_j \right)^2 \right) \quad (12)$$

where $w_{\text{pt}} = 0.1$ and $w_{\text{ang}} = 1$ are weighting factors that were tuned during implementation. In order to use MATHEMATICA's built-in gradient descent optimizer, we transform the variables in f and $\mathcal{C}_j$ into real numbers using substitutions $A = A_x + A_y i$, $B = B_x + B_y i$, etc. The unknown parameters are then

$$\{A_x, A_y, B_x, B_y, C_x, C_y, D_x, D_y, F_x, F_y, G_x, G_y, H_x, H_y, P_{x0}, P_{y0}\}$$
$$\{\phi_j, \psi_j, P_{xj}, P_{yj} \mid j = 1, \ldots, N-1\} \quad (13)$$

Finally, extra constraints were added to ensure the line-of-action passed through the estimated CM and to enforce compactness. The mechanism's line-of-action was constrained to pass through ground pivot B as the CM was estimated to travel vertically below this pivot. Packaging constraints consisted of inequalities specified ad hoc to keep linkage pivots within certain bounds. These extra constraints are placed in the set $\mathcal{D}$.

The optimization problem was set up to minimize f subject to $\{\mathcal{C}_j \mid j = 1, \ldots, N-1\}$ and $\mathcal{D}$. This was accomplished using Mathematica's *InteriorPoint* method with the *FindMinimum* function.

5.2 Energy Storage. In order to accomplish a power modulation factor that exceeds typical values of a series-elastic actuator pushing mass in a gravity field, torque acting on the spring must increase to allow additional energy storage before discharge. We create this additional torque by designing the mechanism to have very low mechanical advantage at the beginning of its stroke, multiplying the effect of the weight of the robot at that point in the motion.

We specify that the mechanism at the low mechanical advantage point produces 125% of body weight at the full stall torque of the motor. Using motor, gear, and weight parameters to be introduced in Sec. 5.5, we compute this mechanical advantage at 1.17 N/Nm. This is a conservative specification to ensure that we have access to the full scope of power modulation. Because the mechanical advantage increases with leg extension, the low mechanical advantage point can be modulated up from this conservative minimum by changing the starting configuration of the linkage.

5.3 Energy Release. In order to release spring energy in a controlled manner, impulsive forces acting on the robot are minimized by designing the ground reaction force to be constant. This was implemented by specifying variable mechanical advantage in a way that a decreasing spring torque at the input link is transformed to a constant force at the foot. For this computation, we neglect the resistance of friction and link inertias, and assume that the input gear is held fixed by the motor at an angle ψ_{eq}; see Fig. 8. During actual operation, additional motion of set point ψ_{eq} may adjust spring torque from this model. The design of variable mechanical advantage begins with the specification of target values for input crank angle $\tilde{\psi}_j$ and output foot translation $\tilde{P}_j$. In this section, we calculate the required mechanical advantage as a function of foot translation.

To solve for the required mechanical advantage, we relate the input torque τ_{in} to the output force F_{out},

$$\tau_{\text{in}} \frac{d\psi}{dy} = F_{\text{out}} \quad (14)$$

where $y = \text{Im}(P)$ is vertical foot translation from reference P_0 and $(d\psi/dy)$ is mechanical advantage. Equation (14) is ideal and does not consider internal friction and inertial forces which require additional information that is not available at this point in the design process. We assume spring torque τ_{in} is defined by Hooke's law, and since F_{out} is a constant force applied over distance Δy, it can be written in terms of the total work W done by the system

$$-k(\psi - \psi_{\text{eq}}) \frac{d\psi}{dy} = \frac{W}{\Delta y} \quad (15)$$

Work W is equal to the initial energy stored in the spring when $\psi = \psi_{\max}$ and $\dot{y} = 0$

$$W = \frac{1}{2} k (\psi_{\max} - \psi_{\text{eq}})^2 \quad (16)$$

Equation (16) is substituted into Eq. (15), and the result is integrated using the initial condition $(y, \psi) = (y_0, \psi_{\max})$, to obtain

$$\psi = g(y) = (\psi_{\max} - \psi_{\text{eq}}) \sqrt{1 - \frac{y - y_0}{\Delta y}} + \psi_{\text{eq}} \quad (17)$$

The function $\psi = g(y)$ describes the coordination between ψ and y to achieve constant force at the foot. Its derivative with respect to y gives the target mechanical advantage as a function of foot translation. For all design iterations presented in this paper, $g(y)$ was specified with parameters $\psi_{\max} = -30$ deg, $\psi_{\text{eq}} = -245$ deg, $y_0 = -0.1008$ m, and $\Delta y = -0.9720$ m.

5.4 Six-Bar Iterations. Execution of the optimization procedure detailed in Sec. 5.1 proceeded interactively. The task specification and packaging constraints were tuned across iterations, adapting the objective for each previous iteration's shortcomings and including multiple required behaviors along the way. Design Iterations II–V produced during six-bar optimization are shown in Fig. 9. Designs were scaled from Iteration I of Fig. 6(*b*) to achieve

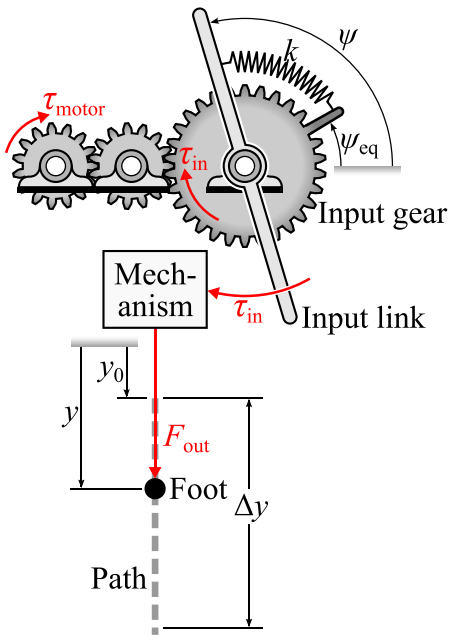

Fig. 8 Mechanical advantage is designed such that a decreasing spring torque is transformed into a constant vertical force pushing off the ground

a 0.162 m stroke. Dots locate task control points $\tilde{P}_j$ where red dots indicate simultaneous specification on $\tilde{\psi}_j$ to institute low mechanical advantage, and blue dots indicate simultaneous specification on $\tilde{\psi}_j$ according to Eq. (17) to institute a constant force at the foot. Packaging constraints are shown in purple with all dimensions in meters.

Early Iterations II and III focused on producing the low mechanical advantage zone at the top of stroke which sacrificed the integrity of the straight line and led to less compact designs. Inequality constraints were placed on long link lengths to improve compactness. Iteration IV introduced more control points to the straight line and coordinated mechanical advantage for a constant force. Iteration V retained precision in the required line and mechanical advantage while making improvements to the stroke ratio and compactness through inequality constraints specified on the ground pivots. The starting design for Iteration II was Iteration I (Fig. 6(*b*)); the starting design for III was II; and the starting design for Iterations IV and V was III. Figure 10(*a*) shows the mechanical advantage profiles of selected iterations.

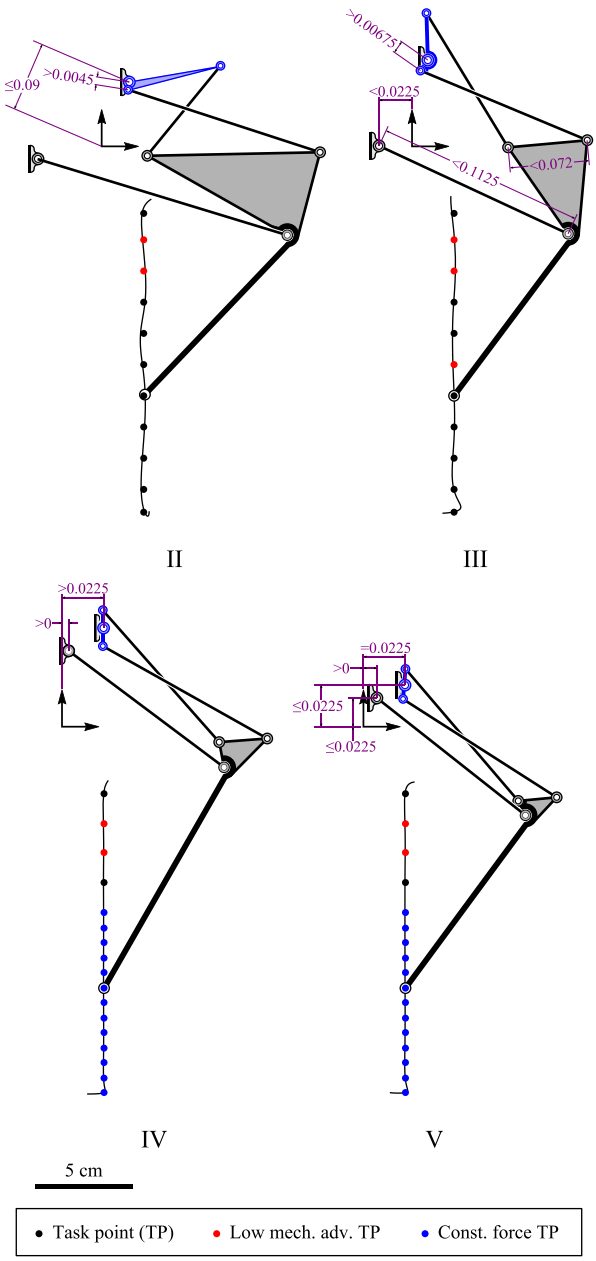

Fig. 9 Design iterations during the optimal design of a six-bar linkage. Input link is colored in blue. Dimensions are in meters.

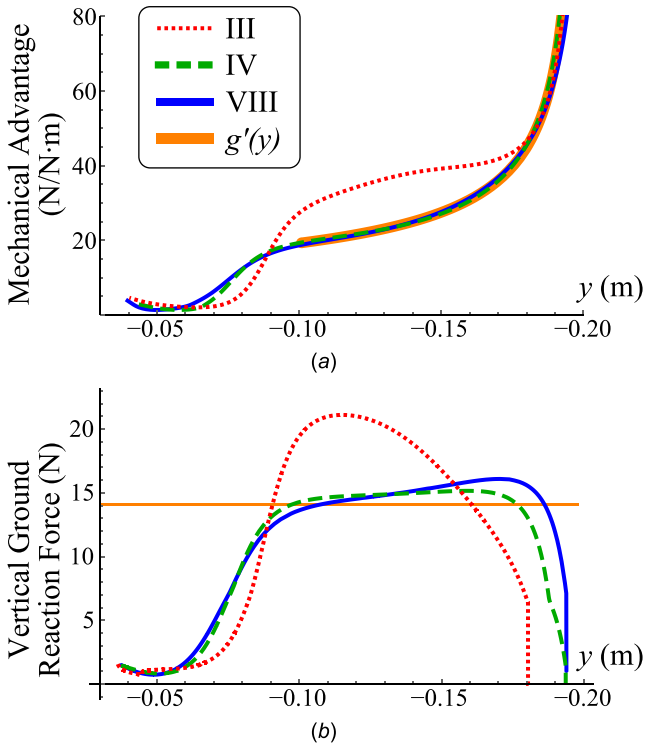

Fig. 10 (*a*) Mechanical advantage as a function of foot translation and (*b*) vertical GRF computed from dynamic simulation for select iterations of Figs. 9 and 14

The satisfaction of required behaviors is summarized across design iterations in Table 1. Each behavior is characterized by a metric that is described here. The ability to trace a straight line (Req. 1) was measured by the absolute value of the area between the actual path and the desired line. The stroke ratio (Req. 2), as defined in Sec. 2.2, is the quotient of vertical CM translation during stance to mechanism length at full extension. The distance between the input pivot and line-of-action (Req. 3) was measured directly. Compactness (Req. 4) was measured by the maximum area of the convex hull defined by the foot point and pivots during mechanism motion. The range of the input link (Req. 5) and the error from desired low mechanical advantage (Req. 6) were measured directly. The error in mechanical advantage from achieving constant force (Req. 7) was measured by comparing the desired constant force to a design's force at the foot. Foot force was computed as a function of stroke y over the range $y_0 \le y \le y_0 + \Delta y$ by multiplying mechanical advantage and ideal spring torque for a frictionless mechanism without inertial loading. The error of this force curve was computed as the absolute value of the area between itself and the desired constant curve. Dividing this area by the spring constant normalizes the metric to a dimensionless quantity we call the *constant force error* in Table 1. The effect of moments exerted on the robot (Req. 8) was measured by the ratio of angular momentum to vertical linear momentum at take-off computed via dynamic simulation (Sec. 5.5). The use of a ratio normalizes for variations in jump velocity.

Minimization of an objective function alone does not encapsulate optimal linkage design due to the existence of branch, circuit, and order defects [97]. Our strategy for avoiding defects is to search in local design spaces defined by defect-free starting designs validated using the process of Plecnik and McCarthy [93]. Wandering too far from these local spaces might incur linkage defects which meant packaging constraints $\mathcal{D}$ could not be specified arbitrarily.

5.5 Dynamic Simulation. Design iterations were analyzed using dynamic simulation to model the robot starting from rest and jumping straight up off the ground. Ground contact was simulated

Table 1 Satisfaction of required behaviors over iterations. Detailed descriptions of metrics are given in Sec. 5.4.

			Six-bar iterations					Eight-bar iterations		
Req.	Metric	Goal	I	II	III	IV	V	VI	VII	VIII
1	Area between lines ($m^2 \times 10^{-6}$)	Min	6.92	130.05	97.47	9.65	15.82	827.51	12.51	19.60
2	Stroke ratio	Max	0.72	0.69	0.65	0.62	0.71	0.68	0.68	0.67
3	Dist. to line-of-action ($m \times 10^{-3}$)	Min	9.53	7.53	13.95	0	0	0	0	0
4	Max convex hull ($m^2 \times 10^{-6}$)	Min	8965	16,332	12,759	10,995	8418	8715	9667	10,202
5	Input rotation (deg)	Max	217	250	278	243	244	203	226	222
6	Low mech. adv. error (N/Nm)	Min	34	0.85	0.81	0.05	0.31	0.24	0.10	0.08
7	Constant force error	Min	4.53	4.85	3.01	0.10	0.07	0.34	0.10	0.17
8	Momentum ratio (Nms/Ns $\times 10^{-3}$)	Min	−3.21	−3.92	−6.06	−11.10	−12.12	1.29	0.60	−0.10

as an asymmetric spring–damper with spring constant 10^4 N/m, damping coefficient 50 Ns/m, and horizontal stick-slip friction with a coefficient of 0.5. The actuator was simulated as a DC motor pushing through a 25:1 gear ratio with a free-running speed of 1240 rad/s, a stall torque of 0.106 Nm, and a torque limit of 0.0294 Nm, allowing a maximum power output of 26.4 W. The simulated robot weighed 0.0700 kg and the spring torque τ_{sp} was computed with a constant of 0.195 Nm/rad. The effect of friction was estimated as an additional torque τ_{fr} acting on the input crank

$$\tau_{fr} = c_1 \tau_{sp} + c_2 \tag{18}$$

with $c_1 = 0.1023$ and $c_2 = 0.0066$ Nm. Equations were solved numerically using MATLAB's built-in ODE solvers.

The simulation of Iteration IV produced a peak jump power 3.2 times the motor's maximum for a jump of 2.1 m. Jump power was computed as the product of the vertical components of the GRF and the CM velocity. The vertical component of the GRF for select iterations is plotted in Fig. 10(*b*) and the time evolution of mechanical energy is plotted in Fig. 11. Simulations indicated the robot accumulated considerable angular momentum on take-off since Req. 8 had not yet been considered; see Fig. 12. Iteration IV rotated at a rate of −35 rad/s after take-off.

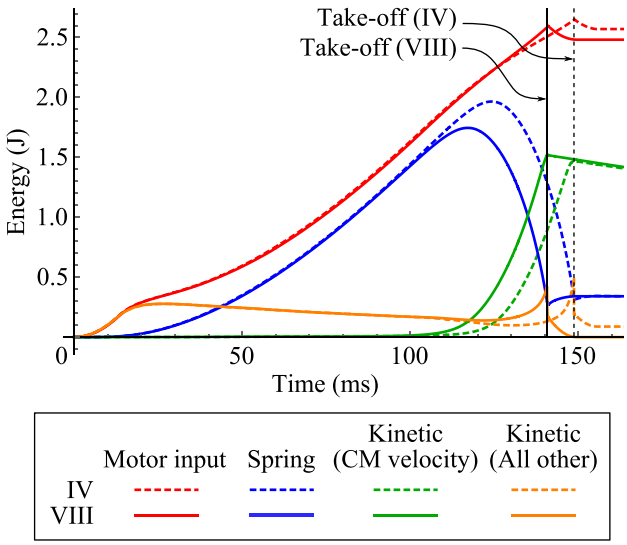

Fig. 11 Time evolution of mechanical energy from simulations of Iterations IV and VIII (the final design)

6 Tuning: Eight-Bar Optimal Design

In order to produce a rotation-free jump, angular momentum about the CM must be zero at the time of take-off. To satisfy Req. 8, we design the angular momentum of the moving links other than the body to approximately sum to zero so that the reaction moment generated on the body is minimized throughout leg extension. This corresponds to vertical travel of the CM along the line-of-action. Preliminary investigations determined that a practical mass balancing scheme of one of the six-bar designs must involve adding more links since existing link locations naturally shifted the robot CM to the right of the line-of-action with all individual link CMs moving clockwise around the robot CM during extension. Therefore, two additional links were added for balance, a new foot link *LMP* constrained by floating link *KM*, forming a single degree-of-freedom eight-bar; see Fig. 13. These new links naturally shift the robot CM closer to the line-of-action, and their individual CMs move counterclockwise around the robot CM. Furthermore, when four-bar subloop *CKML* was specified as a parallelogram (Fig. 14, Iteration VI), link mass was coarsely balanced while modestly disturbing the straight-line (Req. 1), input rotation (Req. 5), and constant force (Req. 7) behaviors, see Table 1. Therefore, Iteration VI was used as a starting design for the optimal synthesis of an eight-bar linkage.

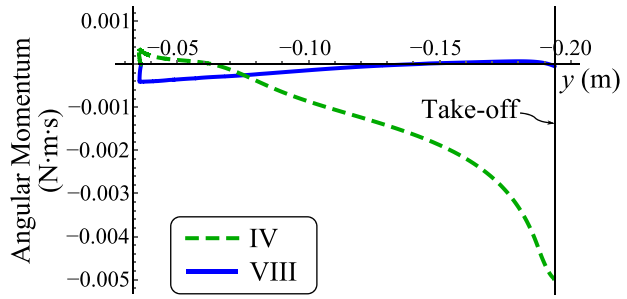

Fig. 12 Angular momentum about the CM during simulated jumps with Iteration IV and Iteration VIII (the final design)

6.1 Formulation. An eight-bar linkage is shown in Fig. 13, consisting of seven moving links *ACK*, *CGHL*, *BDF*, *DG*, *FH*, *KM*, and *LMP*, angularly displaced by ϕ_j, ρ_j, ψ_j, θ_j, μ_j, ν_j, and ζ_j, respectively, in the jth configuration. In addition to the exponential operators introduced in Eq. (2), exponential operators V and Z are introduced to represent rotations of the new links

$$V_j = e^{i\nu_j}, \quad Z_j = e^{i\zeta_j} \tag{19}$$

Design equations are formulated by tracing four kinematic loops of the eight-bar

$$A + Q_j(C - A) + R_j(G - C) = B + S_j(D - B) + T_j(G - D) \tag{20}$$

$$A + Q_j(C - A) + R_j(H - C) = B + S_j(F - B) + U_j(H - F) \tag{21}$$

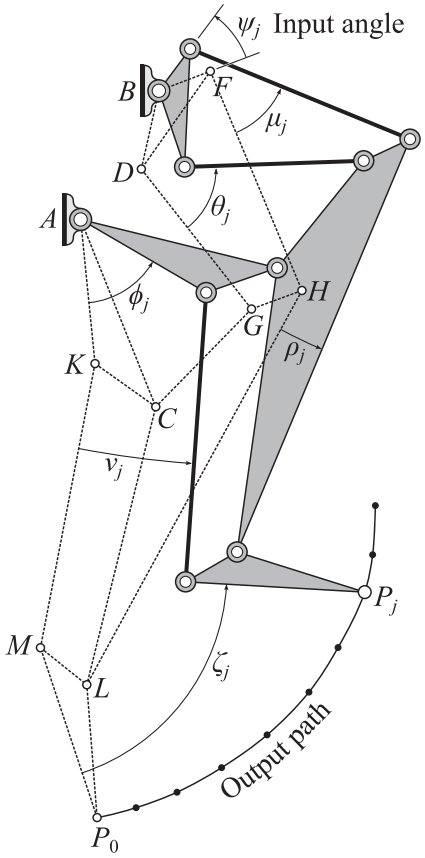

Fig. 13 An eight-bar linkage defined by coordinates *A*, *B*, *C*, *D*, *F*, *G*, *H*, *K*, *L*, *M*, and P_0 drawn in configuration *j*

$$A + Q_j(C - A) + R_j(L - C) + Z_j(P_0 - L) = P_j \tag{22}$$

$$A + Q_j(K - A) + V_j(M - K) + Z_j(P_0 - M) = P_j \tag{23}$$

To facilitate presentation of the design equations, we define intermediate variables,

$$\begin{aligned} d_j &= A - P_j + Q_j(C - A) + Z_j(P_0 - L) \\ f_j &= A - P_j + Q_j(K - A) + Z_j(P_0 - M) \end{aligned} \tag{24}$$

in addition to the intermediate variables of Eq. (6). Exponential operators T_j, U_j, R_j, and V_j are eliminated from Eqs. (20)–(23), respectively, by moving their terms to the right-hand side and multiplying by conjugate equations to obtain

$$(a_j - b_j + R_j(G - C))(\bar{a}_j - \bar{b}_j + \bar{R}_j(\bar{G} - \bar{C})) = (G - D)(\bar{G} - \bar{D}) \tag{25}$$

$$(a_j - c_j + R_j(H - C))(\bar{a}_j - \bar{c}_j + \bar{R}_j(\bar{H} - \bar{C})) = (H - F)(\bar{H} - \bar{F}) \tag{26}$$

$$d_j\bar{d}_j = (L - C)(\bar{L} - \bar{C}) \tag{27}$$

$$f_j\bar{f}_j = (M - K)(\bar{M} - \bar{K}) \tag{28}$$

The variable R_j is eliminated from Eqs. (25) and (26) by solving for R_j in Eq. (22) and substituting to obtain

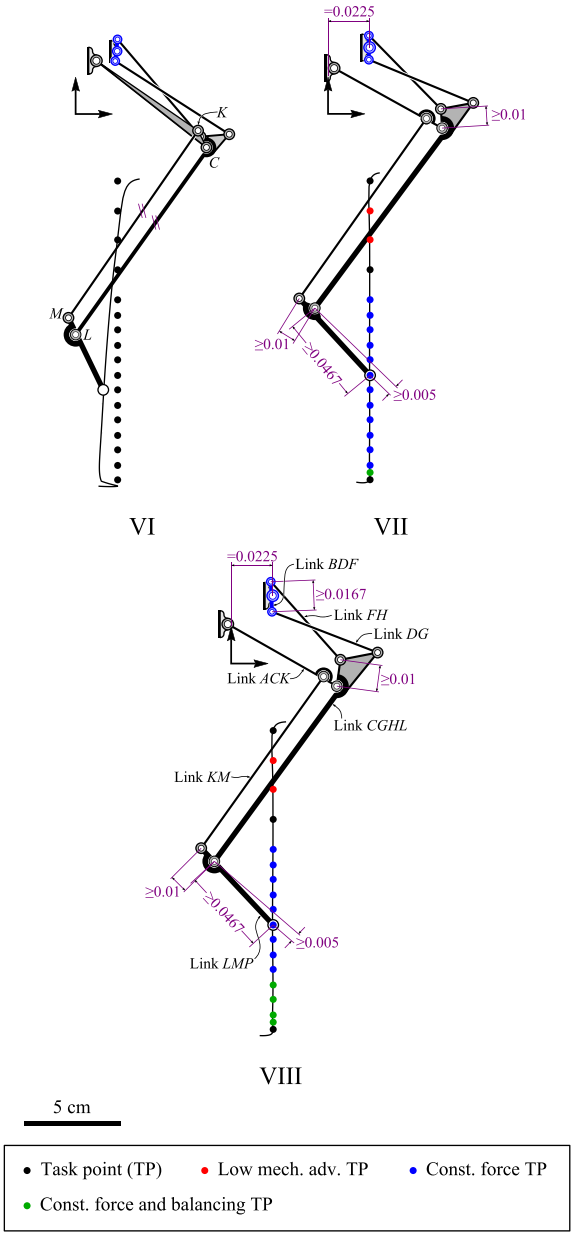

Fig. 14 Design iterations during the optimal design of an eight-bar linkage. Dimensions are in meters.

$$\begin{aligned} &((a_j - b_j)(L - C) - d_j(G - C))((\bar{a}_j - \bar{b}_j)(\bar{L} - \bar{C}) - \bar{d}_j(\bar{G} - \bar{C})) \\ &\quad = (G - D)(\bar{G} - \bar{D})(L - C)(\bar{L} - \bar{C}) \end{aligned} \tag{29}$$

$$\begin{aligned} &((a_j - c_j)(L - C) - d_j(H - C))((\bar{a}_j - \bar{c}_j)(\bar{L} - \bar{C}) - \bar{d}_j(\bar{H} - \bar{C})) \\ &\quad = (H - F)(\bar{H} - \bar{F})(L - C)(\bar{L} - \bar{C}) \end{aligned} \tag{30}$$

Eqns. (27)–(30) represent the constrained geometry of the eight-bar linkage of Fig. 13 in the *j*th configuration. These constraints are used to set up an optimization problem in the same manner as Sec. 5.1 with the objective function modified to accommodate specifications on desired values $\tilde{\zeta}_j$.

6.2 Eight-Bar Iterations. To minimize moments exerted on the body link (Req. 8), specifications of foot angle $\tilde{\zeta}$ were used in tandem with packaging constraints to tune the angular momentum of the moving links. Figure 14 displays design iterations during eight-bar optimal synthesis where control points associated with foot angle balancing are marked with green dots.

Iteration VI coarsely balanced angular momentum with inaccuracies near the bottom of leg extension and disturbances to the straight-line (Req. 1), input rotation (Req. 5), and constant force (Req. 7) behaviors; see Table 1. Iteration VII reinstated these behaviors while specifying a terminal angle of the foot safely away from vertical. A vertical foot moves segments *KM* and *LM* into a collinear configuration referred to by [98] as a "singularity of the first kind," characterized by high link angular velocities for small foot point motions. This makes momentum balancing difficult and unnecessarily increases kinetic energy of the links, which can have parasitic effects on actuation energy. Note that this "first kind of singularity" is different from common use of the word "singularity" which is referred to as the "second kind of singularity" in Ref. [98]. To further limit excess link motion, a packaging constraint was placed on the foot to increase its length, allowing it to reach the bottom of stroke at a lower angular velocity; see Fig. 14. An additional packaging constraint was placed on the foot to ensure pivots *L* and *M* remain above the foot point when this link is near horizontal in its highest position, as in Fig. 1. Several other packaging constraints served to increase distances between particular pivots to make room for bushings.

Iteration VIII improved the balance of angular momentum placing additional specifications on the foot angle near the bottom of extension and increasing the size of the input link to allow room for bushings. Dynamic simulation was run using the specifications of Sec. 5.5, resulting in a power modulation factor of 3.6 for a 2.3 m jump and exhibiting minimal body rotation. The mechanical advantage and the vertical GRF of Iteration VIII are plotted in Fig. 10. Figure 11 compares the time evolution of mechanical energy for Iterations IV and VIII. This figure shows the motor of IV generates slightly more energy operating during an 8 ms longer stance phase; however, VIII generates a greater take-off velocity as energy is not siphoned by rotational motion after take-off. The angular momentum about the CM generated by the ground force during stance is shown in Fig. 12. The simulation of Iteration VIII rotated at −0.33 rad/s after take-off. A comparison of Iteration VIII against all preceding iterations for all required behaviors is shown in Table 1.

Iteration VIII is the final design for the Salto leg mechanism. Its pivot locations in a reference configuration at the top of stroke are

$$\begin{aligned} A &= -0.001830 + 0.021353i, & B &= 0.022500 + 0.036716i \\ C &= 0.060743 + 0.047760i, & D &= 0.031343 + 0.034990i \\ F &= 0.014782 + 0.036869i, & G &= 0.086637 + 0.061279i \\ H &= 0.065686 + 0.061515i, & K &= 0.051913 + 0.045494i \\ L &= -0.023710 - 0.030571i, & M &= -0.033708 - 0.030379i \\ P_0 &= 0.022640 - 0.035994i \end{aligned} \tag{31}$$

with all dimensions in meters. Individual link masses (kg) and CM locations used during simulation are

$$\begin{aligned} m_\phi &= 0.0013, & C_\phi &= 0.034 + 0.035i \\ m_\rho &= 0.0039, & C_\rho &= 0.048 + 0.032i \\ m_\psi &= 0.0010, & C_\psi &= 0.023 + 0.035i \\ m_\theta &= 0.0013, & C_\theta &= 0.060 + 0.048i \\ m_\mu &= 0.00080, & C_\mu &= 0.039 + 0.05i \\ m_\nu &= 0.0016, & C_\nu &= 0.000 + 0.000i \\ m_\zeta &= 0.0022, & C_\zeta &= -0.013 - 0.031i \end{aligned} \tag{32}$$

where subscripts correspond to the link measured by that angle; see Fig. 13.

7 Prototype Design

A prototype of the Salto leg mechanism was built and tested. Dynamic simulation results were used to determine the magnitude and orientation of internal forces generated by the actuator. This information identified which links were solely in tension or compression; links are labeled in Figs. 1 and 14(VIII). Tension links *DG* and *KM* were fabricated as lightweight unidirectional carbon fiber tie rods. Binary links *FH* and *LMP*, and ternary links *ACK* were milled from prefabricated carbon fiber honeycomb sandwich composite plate, using an Othermill[2]. Revolute joint constraints were enforced by precision aluminum rod riding in plain polymer bearings (IGUS JFM-304-05).

Fig. 15 Prototype monopod installed on a universal testing machine

The quaternary link *CGHL* was comprised of molded polymer pieces that house bearing elements, connected by a length of carbon fiber tube. The ternary input link *BDF* was also molded polymer. All of the component molds were fabricated by creating a master mold in machine wax using the Othermill (see footnote 2), and taking a silicone mold from that positive. These fabrication methodologies resulted in a leg mechanism with a net moving component mass of 0.011 kg, which can withstand internal forces up to 200 N.

The torsional spring element was a solid section of latex, as described by Rollinson et al. [99]. It was cut from prefabricated latex tube using a 3D printed jig. The proposed motor is a Scorpion S-1804-1650 BLDC device. The gear reduction is 25:1 with two 5:1 stages.

Our weight budget for the entire robot, complete with actuators, batteries, and control electronics, is 0.085 kg.

8 Results

The Salto prototype mechanism was measured to determine whether its mechanical advantage curve matched the simulated design. A latex torsion spring was attached to the input link and the force at the foot was measured over its stroke with an Instron

[2]Other Machine Company.

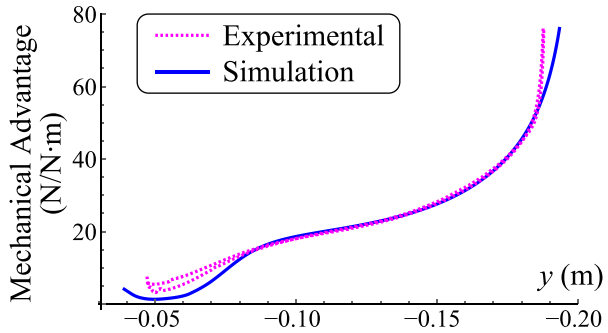

Fig. 16 Mechanical advantage calculated from data measured by a universal testing machine compared to simulation of Iteration VIII. Experimental data show both compression and extension strokes.

universal testing machine; see Fig. 15. For this test, the latex spring was attached such that it deflected maximally to 180 deg instead of the designed value of 245 deg (Sec. 5.3). Also, the latex spring was observed to decrease in stiffness over its deflection and the effect of friction was noted by the presence of a loading/unloading hysteresis loop. To take these effects into account, test data were used to fit a model for spring torque τ_{sp}, and the effect of friction as a torque τ_{fr} on the input

$$\tau_{sp} = -k_\alpha(\psi - \psi_{eq})^\alpha \tag{33}$$

$$\tau_{fr} = c\tau_{sp} \tag{34}$$

where $k_\alpha = 0.203$ Nm/rad, $\alpha = 0.768$, and $c = 0.175$. Note that for $\alpha > 0$, the average stiffness of the spring for a deflection of $\Delta\psi$ is $\Delta\psi^{\alpha-1} = 77\%$ of the value of coefficient k_α as the spring monotonically softens over its stroke. The mechanical advantage of the prototype was calculated as

$$\text{MA} = \frac{F_{out}}{\tau_{sp} \pm \tau_{fr}} \tag{35}$$

where the $\pm$ sign corresponds to compression and extension strokes of the hysteresis loop. Experimental data plotted alongside the simulated curve of Salto are shown in Fig. 16. Discrepancies may be due to joint slop, link deflection, unmodeled friction, or manufacturing inaccuracies.

Spring-powered test jumps of the Salto leg prototype were also recorded using a Mega Speed HHC X7 500 fps camera and PROANALYST motion tracking software. For each jump, the 0.045 kg prototype was held to the ground with its spring wound to approximately 180 deg and the leg slightly past its low mechanical advantage region, then released. For a characteristic jump, the prototype traveled a vertical distance of 1.00 m, pitching forward to approximately 2 deg at its apogee; see Fig 17. The prototype also experienced approximately 180 deg of yaw about its long axis due to out-of-plane asymmetries which are out of the scope of this paper.

Motor-powered experiments that demonstrate the capability of series-elastic power modulation to produce high amplitude, high frequency jumps are contained in Ref. [1].

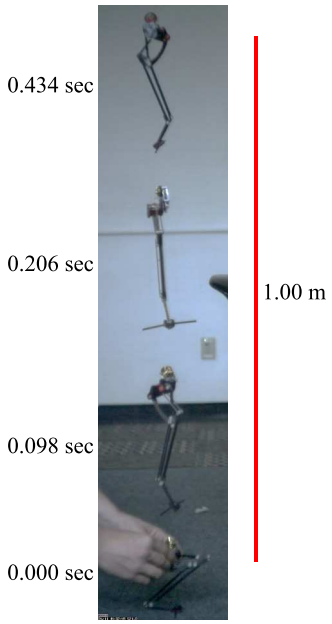

Fig. 17 Composition of high speed footage for a spring-powered jump of 0.995 m

9 Conclusion

We described the synthesis of a leg mechanism for the monopedal robot, Salto, to perform controllable, high-powered jumps. The synthesis procedure involved design exploration followed by detailed kinematic tuning. The first phase generated an atlas of six-bars that produced a set of primary behaviors, and the second phase performed optimal synthesis to simultaneously produce a set of more intricate behaviors, including mass balancing which prompted the addition of extra links making the final design an eight-bar linkage. A variable mechanical advantage curve was designed into the mechanism's geometry to achieve a power modulation factor of 3.6 in simulation. A prototype was constructed, its mechanical advantage was verified on a universal testing machine, and its minimization of pitch velocities was verified with high speed video of meter high jumps.

Acknowledgment

This material is based upon work supported by the National Science Foundation under Grant Nos. CMMI-1549667 and DGE-0903711, the Graduate Research Fellowship Program, as well as the United States Army Research Laboratory under the Micro Autonomous Science and Technology Collaborative Technology Alliance. All authors of this paper are inventors on a patent application submitted by the University of California that covers the jumping system and associated software described in this paper.

References

[1] Haldane, D. W., Plecnik, M. M., Yim, J. K., and Fearing, R. S., 2016, "Robotic Vertical Jumping Agility Via Series-Elastic Power Modulation," Sci. Rob., (in Press).
[2] Martin, Y. C., 1992, "3D Database Searching in Drug Design," J. Med. Chem., **35**(12), pp. 2145–2154.
[3] Leach, A. R., Bradshaw, J., Green, D. V., Hann, M. M., and Delany, J. J., 1999, "Implementation of a System for Reagent Selection and Library Enumeration, Profiling, and Design," J. Chem. Inf. Comput. Sci., **39**(6), pp. 1161–1172.
[4] Feuston, B. P., Chakravorty, S. J., Conway, J. F., Culberson, J. C., Forbes, J., Kraker, B., Lennon, P. A., Lindsley, C., McGaughey, G. B., Mosley, R., Sheridan, R. P., Valenciano, M., and Kearsley, S. K., 2005, "Web Enabling Technology for the Design, Enumeration, Optimization and Tracking of Compound Libraries," Curr. Top. Med. Chem., **5**(8), pp. 773–783.
[5] Welsch, M. E., Snyder, S. A., and Stockwell, B. R., 2010, "Privileged Scaffolds for Library Design and Drug Discovery," Curr. Opin. Chem. Biol., **14**(3), pp. 347–361.
[6] Du, H., Fuh, R. A., Li, J., Corkan, A., and Lindsey, J. S., 1998, "PhotochemCAD: A Computer-Aided Design and Research Tool in Photochemistry," Photochem. Photobiol., **68**(2), pp. 141–142.
[7] Wang, G., Li, X., and Wang, Z., 2009, "APD2: The Updated Antimicrobial Peptide Database and Its Application in Peptide Design," Nucleic Acids Res., **37**(1), pp. D933–D937.
[8] Gedye, D., and Katz, R., 1988, "Browsing in Chip Design Database," 25th ACM/IEEE Design Automation Conference, pp. 269–274.

[9] Kravets, V. N., and Kudva, P., 2004, "Implicit Enumeration of Structural Changes in Circuit Optimization," 41st Annual Design Automation Conference (DAC), San Diego, CA, June 7–11, pp. 438–441.
[10] Catalano, M. G., Schiavi, R., and Bicchi, A., 2010, "Mechanism Design for Variable Stiffness Actuation Based on Enumeration and Analysis of Performance," 2010 IEEE International Conference on Robotics and Automation (ICRA), Anchorage, AK, May 3–8, pp. 3285–3291.
[11] Kim, J. S., Kim, N. P., and Han, S. H., 2005, "Optimal Stiffness Design of Composite Laminates for a Train Carbody by an Expert System and Enumeration Method," Compos. Struct., **68**(2), pp. 147–156.
[12] de Keijzer, B., Klos, T., and Zhang, Y., 2010, "Enumeration and Exact Design of Weighted Voting Games," 9th International Conference on Autonomous Agents and Multiagent Systems (AAMAS), Toronto, ON, Canada, May 9–14, Vol. 1, pp. 391–398.
[13] Ma, X., Soh, A. K., and Wang, B., 2004, "A Design Database for Moulded Pulp Packaging Structure," Packag. Technol. Sci., **17**(4), pp. 193–204.
[14] Doucette, J., He, D., Grover, W. D., and Yang, O., 2003, "Algorithmic Approaches for Efficient Enumeration of Candidate p-Cycles and Capacited p-Cycle Network Design," Fourth International Workshop on Design of Reliable Communication Networks 2003, (DRCN), Alberta, Canada, Oct. 19–22, pp. 212–220.
[15] Orlowski, S., Wessäly, R., Pióro, M., and Tomaszewski, A., 2010, "SNDlib 1.0–Survivable Network Design Library," Networks, **55**(3), pp. 276–286.
[16] Page, G. P., Edwards, J. W., Gadbury, G. L., Yelisetti, P., Wang, J., Trivedi, P., and Allison, D. B., 2006, "The PowerAtlas: A Power and Sample Size Atlas for Microarray Experimental Design and Research," BMC Bioinf., **7**(1), pp. 1–9.
[17] Brown, H. T., 1871, *Five Hundred and Seven Mechanical Movements*, Brown, Coombs & Co., New York.
[18] Schröder, J., 1899, *Illustrationen von Unterrichts—Modellen und Apparaten*. Polytechnisches Arbeits-Institut, Darmstadt, Germany.
[19] Voigt, G., 1907, *Kinematische Modelle Nach Professor Reuleaux, Verzeichnis I,II*, Gustav Voigt Mechanische Werkstatt, Berlin.
[20] Hrones, J. A., and Nelson, G. I., 1951, *Analysis of the Four-bar Linkage*, Massachusetts Institute of Technology/Wiley, Cambridge, MA/New York.
[21] Todd, P., Mueller, D., and Fichter, E., 2014, *Atlas of the Four-Bar Linkage*, 2nd ed., Saltire Software, Tigard, OR.
[22] Moon, F. C., 2004, "The Reuleaux Models: Creating an International Digital Library of Kinematics History," International Symposium on History of Machines and Mechanisms, M. Ceccarelli, ed., Kluwer Academic Publishers, New York, pp. 331–344.
[23] Yan, H. S., Huang, H. H., and Kuo, C. H., 2007, "Historic Mechanism Teaching Models in Taiwan," 12th IFToMM World Congress on Mechanism and Machine Science, Besancon, France, June 18–21.
[24] Henkel, V., Brix, T., and Falke, S., 2013, "The Digital Mechanism and Gear Library Supports Design Engineers in Finding Ideas for Design Solutions in the Field of Motion Systems," 18th International Conference, Mechanika, Kaunus, Lithuania, Apr. 4–5, pp. 87–92.
[25] Raghavan, M., 1991, "An Atlas of Linkages for Independent Suspensions," SAE Technical Paper No. 911925.
[26] Belfiore, N. P., and Pennestrí, E., 1997, "An Atlas of Linkage-Type Robotic Grippers," Mech. Mach. Theory, **32**(7), pp. 811–833.
[27] Yan, H. S., 1998, *Creative Design of Mechanical Devices*, Springer, Singapore.
[28] Tsai, L. W., 2001, *Mechanism Design: Enumeration of Kinematic Structures According to Function*. CRC Press, Boca Raton, FL.
[29] Galletti, C. U., and Giannotti, E. I., 1981, "Interactive Computer System for the Functional Design of Mechanisms," Comput.-Aided Des., **13**(3), pp. 159–163.
[30] Chu, J., and Sun, J., 2010, "Numerical Atlas Method for Path Generation of Spherical Four-Bar Mechanism," Mech. Mach. Theory, **45**(6), pp. 867–879.
[31] Mullineux, G., 2011, "Atlas of Spherical Four-Bar Mechanisms," Mech. Mach. Theory, **46**(11), pp. 1811–1823.
[32] Chu, J., and Sun, J., 2010, "A New Approach to Dimension Synthesis of Spatial Four-Bar Linkage Through Numerical Atlas Method," ASME J. Mech. Rob., **2**(4), p. 041004.
[33] Zhang, C., Norton, R. L., and Hammonds, T., 1984, "Optimization of Parameters for Specified Path Generation Using an Atlas of Coupler Curves of Geared Five-Bar Linkages," Mech. Mach. Theory, **19**(6), pp. 459–466.
[34] Coros, S., Thomaszewski, B., Noris, G., Sueda, S., Forberg, M., Sumner, R. W., Matusik, W., and Bickel, B., 2013, "Computational Design of Mechanical Characters," SIGGRAPH Conference Proceedings, Hong King, Nov. 19–22, Vol. 32 p. 83.
[35] Unruh, V., and Krishnaswami, P., 1995, "A Computer-Aided Design Technique for Semi-Automated Infinite Point Coupler Curve Synthesis of Four-Bar Linkages," ASME J. Mech. Des., **117**(1), pp. 143–149.
[36] Yu, H., Zhao, Y., and Xu, D., 2015, "A Path Synthesis Method of Planar Hinge Four-Bar Linkage," J. Harbin Inst. Technol., **47**(1), pp. 40–47.
[37] McGarva, J. R., 1994, "Rapid Search and Selection of Path Generating Mechanisms From a Library," Mech. Mach. Theory, **29**(2), pp. 223–235.
[38] Singh, B., Matthews, J., Mullineux, G., and Medland, A. J., 2008, "Design Catalogues for Mechanism Selection," International Design Conference (DESIGN 2008), Dubrovnik, Croatia, May 19–22, pp. 673–680.
[39] Primrose, E. J., Freudenstein, F., and Roth, B., 1967, "Six-Bar Motion—II: The Stephenson-1 and Stephenson-2 Mechanisms," Arch. Ration. Mech. Anal., **24**(1), pp. 42–72.
[40] Fox, R. L., and Willmert, K. D., 1967, "Optimum Design of Curve-Generating Linkages With Inequality Constraints," Trans. ASME, **89**(1), pp. 144–151.
[41] Bagci, C., and Burke, D., 1993, "Optimum Synthesis of Coupler Curve and Uniform Rotary Motion Driven Multiloop Mechanisms Generating Complex Output Motions," ASME J. Mech. Des., **115**(4), pp. 967–977.
[42] Raibert, M. H., Brown, H. B., Jr., and Chepponis, M., 1984, "Experiments in Balance With a 3D one-Legged Hopping Machine," Int. J. Rob. Res., **3**(2), pp. 75–92.
[43] Chen, K., Chen, D., Zhang, Z., and Wang, M., 2016, "Jumping Robot With Initial Body Posture Adjustment and a Self-Righting Mechanism," Int. J. Adv. Rob. Syst., **13**(3), p. 127.
[44] Nguyen, Q., and Park, H. C., 2012, "Design and Demonstration of a Locust-Like Jumping Mechanism for Small-Scale Robots," J. Bionic Eng., **9**(3), pp. 271–281.
[45] Papantoniou, K. V., 1991, "Electromechanical Design for an Electrically Powered, Actively Balanced One Leg Planar Robot," 1991 IEEE/RSJ International Workshop on Intelligent Robots and Systems, (IROS), Osaka, Japan, Nov. 3–5, pp. 1553–1560.
[46] Kikuchi, F., Ota, Y., and Hirose, S., 2003, "Basic Performance Experiments for Jumping Quadruped," IEEE/RSJ International Conference on Intelligent Robots and Systems, Las Vegas, Oct. 27–31, pp. 3378–3383.
[47] Lambrecht, B. G. A., Horchler, A. D., and Quinn, R. D., 2005, "A Small, Insect-Inspired Robot That Runs and Jumps," IEEE International Conference on Robotics and Automation, Barcelona, Spain, Apr. 18–22, pp. 1240–1245.
[48] Tae, W., Kim, S., and Kwak, Y., 2009, "Development of Jumping Mechanism for Small Reconnaissance Robot," J. Korea Inst. Mil. Sci. Technol., **12**(5), pp. 563–570.
[49] Noh, M., Kim, S. W., An, S., Koh, J., and Cho, K., 2012, "Flea-Inspired Catapult Mechanism for Miniature Jumping Robots," IEEE Trans. Rob., **28**(5), pp. 1007–1018.
[50] Chen, D., Yin, J., Huang, Y., Zhao, K., and Wang, T., 2013, "A Hopping-Righting Mechanism Analysis and Design of the Mobile Robot," J. Braz. Soc. Mech. Sci. Eng., **35**(4), pp. 469–478.
[51] Woodward, M. A., and Sitti, M., 2014, "Multimo-Bat: A Biologically Inspired Integrated Jumping-Gliding Robot," Int. J. Rob. Res., **33**(12), pp. 1511–1529.
[52] Driessen, J. J. M., 2015, "Machine and Behaviour co-Design of a Powerful Minimally Actuated Hopping Robot," Master's thesis, Delft University of Technology, Delft, The Netherlands.
[53] Jung, G., Casarez, C. S., Jung, S., Fearing, R. S., and Cho, K., 2016, "An Integrated Jumping-Crawling Robot Using Height-Adjustable Jumping Module," 2016 IEEE International Conference on Robotics and Automation (ICRA), Stockholm, Sweden, May 16–21 pp. 4680–4685.
[54] Lee, W., and Raibert, M., 1991, "Control of Hoof Rolling in an Articulated Leg," 1991 IEEE International Conference on Robotics and Automation (ICRA), Sacramento, CA, Apr. 9–11, pp. 1386–1391.
[55] Scarfogliero, U., Stefanini, C., and Dario, P., 2009, "The Use of Compliant Joints and Elastic Energy Storage in Bio-Inspired Legged Robots," Mech. Mach. Theory, **44**(3), pp. 580–590.
[56] Kovač, M., 2010, "Bioinspired Jumping Locomotion for Miniature Robotics," Ph.D thesis, École Polytechnique Fédérale de Lausanne, Lausanne, Switzerland.
[57] Zhang, J., Song, G., Li, Y., Qiao, G., Song, A., and Wang, A., 2013, "A Bio-Inspired Jumping Robot: Modeling, Simulation, Design, and Experimental Results," Mechatronics, **23**(8), pp. 1123–1140.
[58] Jun, B. R., Kim, Y. J., and Jung, S., 2016, "Design and Control of Jumping Mechanism for a Kangaroo-Inspired Robot," 2016 IEEE RAS/EMBS International Conference on Biomedical Robotics and Biomechatronics (BioRob), Singapore, June 26–29, pp. 436–440.
[59] Tachella, R., 2016, "Design and Development of a Salticid Inspired Jumping Robot," Master's thesis, Oregon State University, Corvallis, OR.
[60] Li, F., Liu, W., Fu, X., Bonsignori, G., Scarfogliero, U., Stefanini, C., and Dario, P., 2012, "Jumping Like an Insect: Design and Dynamic Optimization of a Jumping Mini Robot Based on Bio-Mimetic Inspiration," Mechatronics, **22**(2), pp. 167–176.
[61] Wei, D., and Ge, W., 2014, "Research on one Bio-Inspired Jumping Locomotion Robot for Search and Rescue," Int. J. Adv. Rob. Syst., **11**(168), pp. 1–10.
[62] Kenneally, G., De, A., and Koditschek, D. E., 2015, "Leg Design for Energy Management in an Electromechanical Robot," 2015 IEEE/RSJ International Conference on Intelligent Robots and Systems (IROS), Hamburg, Germany, Sept. 28–Oct. 2, pp. 5712–5718.
[63] Fiorini, P., and Burdick, J., 2003, "The Development of Hopping Capabilities for Small Robots," Auton. Rob., **14**(2), pp. 239–254.
[64] Song, G., Yin, K., Zhou, Y., and Cheng, X., 2009, "A Surveillance Robot With Hopping Capabilities for Home Security," IEEE Trans. Consum. Electron., **55**(4), pp. 2034–2039.
[65] Zhao, J., 2015. "Biologically Inspired Approach for Robot Design and Control," Ph.D dissertation, Michigan State University, East Lansing, MI.
[66] Ho, T., and Lee, S., 2015, "Development of a Minimally Actuated Jumping-Rolling Robot," Int. J. Adv. Rob. Syst., **12**(45).
[67] Okada, M., and Takeda, Y., 2012, "Optimal Design of Nonlinear Profile of Gear Ratio Using Non-Circular Gear for Jumping Robot," IEEE International Conference on Robotics and Automation, St. Paul, MN, May 14–18, pp. 1958–1963.
[68] Zeglin, G., 1991, "Uniroo: A One Legged Dynamic Hopping Robot," B.S., thesis, Massachusetts Institute of Technology, Cambridge, MA.
[69] Hyon, S. H., and Mita, T., 2002, "Development of a Biologically Inspired Hopping Robot—"Kenken"," 2002 IEEE International Conference on Robotics and Automation (ICRA), Washington, D.C., May 15, pp. 3984–3991.
[70] Oshima, T., Momose, N., Koyanagi, K., Matsuno, T., and Fujikawa, T., 2007, "Jumping Mechanism Imitating Vertebrate by the Mechanical Function of Bi-Articular Muscle," IEEE International Conference on Mechatronics and Automation, Harbin, China, Aug. 5–8, pp. 1920–1925.
[71] Igarashi, A., and Mikami, S., 2014, "Frog-Like Robot With Jump and Walk Mechanism for Locomotion on Rough Terrain," 2014 International Conference

on Control Automation Robotics & Vision (ICARCV), Singapore, Dec. 10–12, pp. 1788–1791.
[72] Zaitsev, V., Gvirsman, O., Hanan, U. B., Weiss, A., Ayali, A., and Kosa, G., 2015, "A Locust-Inspired Miniature Jumping Robot," Bioinspiration & Biomimetics, **10**(6), p. 066012.
[73] Koh, J., Jung, S., Wood, R. J., and Cho, K., 2013, "A Jumping Robotic Insect Based on a Torque Reversal Catapult Mechanism," 2013 IEEE/RSJ International Conference on Intelligent Robots and Systems (IROS), Tokyo, Nov. 3–7, pp. 3796–3801.
[74] Jung, S., Jung, G., Koh, J., Lee, D., and Cho, K., 2015, "Fabrication of Composite and Sheet Metal Laminated Bistable Jumping Mechanism," ASME J. Mech. Rob., **7**(2), p. 021010.
[75] Yamada, A., Mameda, H., Fujimoto, H., and Mochiyama, H., 2010, "A Compact Jumping Robot Based on Continuous Snap-Through Buckling for Hybrid Environment," 13th International Conference on Climbing and Walking Robots and the Support Technologies for Mobile Machines, CLAWAR 2010, Nagoya, Japan, Aug. 31–Sept. 3, pp. 245–252.
[76] Tsuda, T., Mochiyama, H., and Fujimoto, H., 2012, "Quick Stair-Climbing Using Snap-Through Buckling of Closed Elastica," 2012 International Symposium on Micro-NanoMechatronics and Human Science (IEEE), Nagoya, Japan, Nov. 4–7, pp. 368–373.
[77] Zeglin, G., 1999, "The Bow Leg Hopping Robot," Ph.D dissertation, Carnegie Mellon University, Pittsburgh, PA.
[78] Stoeter, S. A., and Papanikolopoulos, N., 2006, "Kinematic Motion Model for Jumping Scout Robots," IEEE Trans. Rob., **22**(2), pp. 397–402.
[79] Armour, R., Paskins, K., Bowyer, A., Vincent, J., and Megill, W., 2007, "Jumping Robots: A Biomimetic Solution to Locomotion Across Rough Terrain," Bioinspiration & Biomimetics, **2**(3), pp. S65–S82.
[80] Miyazaki, M., and Hirai, S., 2008, "Jumping Via Robot Body Deformation—Mechanics and Mechanism for Higher Jumping," 11th International Conference on Climbing and Walking Robots and the Support Technologies for Mobile Machines, CLAWAR 2008, Coimbra, Portugal, Sept. 8–10, pp. 373–380.
[81] Dubowsky, S., Kesner, S., Plante, J., and Boston, P., 2008, "Hopping Mobility Concept for Search and Rescue Robots," Ind. Rob.: Int. J., **35**(3), pp. 238–245.
[82] Gerratt, A. P., and Bergbreiter, S., 2013, "Incorporating Compliant Elastomers for Jumping Locomotion in Microrobots," Smart Mater. Struct., **22**(1), p. 014010.
[83] Zhao, J., Yan, W., Xi, N., Mutka, M. W., and Xiao, L., 2014, "A Miniature 25 Grams Running and Jumping Robot," 2014 IEEE International Conference on Robotics and Automation, ICRA, Hong Kong, May 31–June 7, pp. 5115–5120.
[84] Ni, F., Rojas, D., Tang, K., Cai, L., and Asfour, T., 2015, "A Jumping Robot Using Soft Pneumatic Actuator," 2015 IEEE International Conference on Robotics and Automation, ICRA, Seattle, WA, May 26–30, pp. 3154–3159.
[85] Brill, A. L., De, A., Johnson, A. M., and Koditschek, D. E., 2015, "Tail-Assisted Rigid and Compliant Legged Leaping," IEEE/RSJ International Conference on Intelligent Robots and Systems, Hamburg, Germany, Sept. 28–Oct. 2, pp. 6304–6311.
[86] Fankhauser, P., Hutter, M., Gehring, C., Bloesch, M., Hoepflinger, M. A., and Siegwart, R., 2013, "Reinforcement Learning of Single Legged Locomotion," IEEE/RSJ International Conference on Intelligent Robots and Systems, Tokyo, Nov. 3–7, pp. 188–193.
[87] Bonsignori, G., Stefanini, C., Scarfogliero, U., Mintchev, S., Benelli, G., and Dario, P., 2013, "The Green Leafhopper, *Cicadella Viridis* (Hemiptera, Auchenorrhyncha, Cicadellidae), Jumps With Near-Constant Acceleration," J. Exp. Biol., **216**(7), pp. 1270–1279.
[88] Aerts, P., 1998, "Vertical Jumping in *Galago Senegalensis*: the Quest for an Obligate Mechanical Power Amplifier," Philos. Trans. R. Soc. London B, **353**(1375), pp. 1607–1620.
[89] Galantis, A., and Woledge, R. C., 2003, "The Theoretical Limits to the Power Output of a Muscle-Tendon Complex With Inertial and Gravitational Loads," Proc. R. Soc. B, **270**(1523), pp. 1493–1498.
[90] Haldane, D. W., Plecnik, M., Yim, J. K., and Fearing, R. S., 2016, "A Power Modulating Leg Mechanism for Monopedal Hopping," 2016 IEEE/RSJ International Conference on Intelligent Robots and Systems, IROS, Daejeon, Korea, Oct. 9–14, pp. 4757–4767.
[91] Gero, J. S., 1990, "Design Prototypes: A Knowledge Representation Schema for Design," AI Mag., **11**(4), pp. 26–36.
[92] Nolle, H., 1974, "Linkage Coupler Curve Synthesis: A Historical Review–I. Developments up to 1875," Mech. Mach. Theory, **9**(2), pp. 147–168.
[93] Plecnik, M., and McCarthy, J. M., 2016, "Design of Stephenson Linkages That Guide a Point Along a Specified Trajectory," Mech. Mach. Theory, **96**(1), pp. 38–51.
[94] Plecnik, M., and McCarthy, J. M., 2015, "Computational Design of Stephenson II Six-Bar Function Generators for 11 Accuracy Points," ASME J. Mech. Rob., **8**(1), p. 011017.
[95] Plecnik, M., and McCarthy, J. M., 2016, "Kinematic Synthesis of Stephenson III Six-Bar Function Generators," Mech. Mach. Theory, **97**, pp. 112–126.
[96] Dijksman, E. A., 1994. "True Straight-Line Linkages Having a Rectilinear Translating Bar," *Advances in Robot Kinematics and Computational Geometry*, J. Lenarčič and B. Ravani, eds., Kluwer Academic Publishers, Dordrecht, The Netherlands, pp. 411–420.
[97] Balli, S. S., and Chand, S., 2002, "Defects in Link Mechanisms and Solution Rectification," Mech. Mach. Theory, **37**(9), pp. 851–876.
[98] Gosselin, C., and Angeles, J., 1990, "Singularity Analysis of Closed-Loop Kinematic Chains," IEEE Trans. Rob. Autom., **6**(3), pp. 281–290.
[99] Rollinson, D., Ford, S., Brown, B., and Choset, H., 2013, "Design and Modeling of a Series Elastic Element for Snake Robots," ASME Paper No. DSCC2013-3875.